Journal of The Electrochemical Society, **159** (7) D418-D424 (2012)
0013-4651/2012/159(7)/D418/7/$28.00 © The Electrochemical Society

Cathodic Deposition of TiO_2: Effects of H_2O_2 and Deposition Modes

Chi-Chang Hu,*,z Huan-Ching Hsu, and Kuo-Hsin Chang

Department of Chemical Engineering, National Tsing Hua University, Hsin-Chu 30013, Taiwan

Cathodic deposition of titanium dioxide (TiO_2) from two plating solutions with H_2O_2 and $NaNO_3$ as their respective oxidants for converting Ti(III) into Ti(IV) are systematically compared. From the electrochemical quartz crystal microbalance (EQCM) and mass loading studies, the deposition solution containing H_2O_2, denoted as bath A, exhibits a higher rate of TiO_2 deposition in comparison with the solution containing $NaNO_3$, denoted as bath B, probably due to the formation of Ti(IV) oxy-hydroxyl species in bath A. However, the surface morphology and crystalline structure of annealed TiO_2 deposits are not significantly affected by using different deposition baths. TiO_2 deposits have been successfully electroplated onto Ti substrates from both baths under the dual-electrode deposition mode. The surface morphology of TiO_2 is significantly influenced by the deposition methods including galvanostatic, potentiostatic, and pulse-rest modes. Finally, uniform porous morphologies of TiO_2 in cm^2 scale are controllable by varying the pulse-rest deposition variables (e.g., pulse frequency and duty percentage) due to its unique advantages such as excellent adhesion, good uniformity, and controllable particle size of TiO_2.
 [DOI: 10.1149/2.026207jes]

Manuscript submitted February 8, 2012; revised manuscript received March 19, 2012. Published July 17, 2012.

In recent years, TiO_2 has shown a great deal of attractive properties and has been intensively investigated for applications in dye-sensitized solar cells (DSSC), photocatalysts, electrochromic devices, gas sensors, and water purification.[1–3] TiO_2 can be divided into three main crystalline phases: anatase, rutile, and brookite. Among them, TiO_2 in the anatase phase (A-TiO_2) shows relatively high photo-activity and chemical stability. Furthermore, A-TiO_2 is the most used phase for photovoltaic applications because its conduction band is similar to the lowest unoccupied molecular orbit of dyes.[4,5]

TiO_2 films can be synthesized using a wide variety of methods like chemical vapor deposition, so-gel, hydrothermal, electrospinning, anodization, and electrodeposition.[3,6–8] In these techniques, electrochemical deposition showed several advantages such as thickness control, uniformity, low cost, and a simple process.[9] The most common methods in electrochemical deposition are anodic deposition, cathodic deposition, and potentiodynamic deposition.[9–19] Several transition metal oxides are fabricated by cathodic deposition, e.g., $Ni(OH)_2$,[20] $Co(OH)_2$,[21] ZnO,[22–24] TiO_2,[25,26] SnO_2,[27] etc. The mechanism can be simply described as follow:

$$2H_2O + 2e^- \rightarrow H_2 + 2OH^- \quad (1)$$

$$2NO_3^- + 6H_2O + 10e \rightarrow N_2 + 12OH^- \quad (2)$$

$$NO_3^- + 6H_2O + 8e^- \rightarrow NH_3 + 9OH^- \quad (3)$$

$$M^{n+} + nOH^- \rightarrow \text{Metal hydroxide} \xrightarrow{dehydration} \text{Metal oxide} \quad (4)$$

Equations (1)–(3) are the common reduction routes for generating hydroxyl ions at the vicinity of cathodes and metal hydroxides precipitate onto the substrate by the combination of metal ions and hydroxyl ions generated at the vicinity of cathodes (equation (4)). Obviously, the formation of OH^- is the key step in preparing metal hydroxides and dehydration of the hydroxide precipitates results in the formation of oxo bonds causing the generation of the final oxides. Based on the above idea, several researchers have investigated the cathodic deposition of TiO_2 by using NO_3^- and water as the source of OH^-.

In our previous work,[28,29] a simple solution containing $TiCl_3$ and $NaNO_3$ was developed for the cathodic deposition of porous A-TiO_2 films, which showed a much faster deposition rate in comparison with several previous deposition baths, due to the electrocatalytic activity of already deposited TiO_2 for the NO_3^- reduction in generating extensive OH^- at the cathode vicinity. In this simple plating bath, NO_3^- works as the oxidant for Ti(IV) formation and the source for OH^- generation. Since hydrogen peroxide (H_2O_2) has been used to prepare several deposition baths for the cathodic deposition of TiO_2,[12,30–32] the solution containing $TiCl_3$ and H_2O_2 in the stoichiometric ratio can be a potential bath for cathodic deposition of porous A-TiO_2. In addition, the redox reactions between H_2O_2 and metal ions will generate hydroxyl radicals ($OH\cdot$) according to the Fenton reaction mechanism;[33–35] i.e., transition metal ions catalyze the decompositon of H_2O_2 and creat $OH\cdot$:

$$M^{n+} + H_2O_2 \rightarrow M^{(n+1)+} + OH^- + OH\cdot \quad (5)$$

$$M^{n+} + OH\cdot \rightarrow M^{(n+1)+} + OH^- \quad (6)$$

The coordination between metallic ions and OH^- may be favorable for the formation of hydroxide precipitates. Based on this consideration, this work employs H_2O_2 as a new oxidant for oxidizing Ti(III) to Ti(IV) while NO_3^- reduction is used to generate OH^-.

Due to the considerations of cheap equipments, easy mass production, and uniform electric field of a dual-electrode electrochemical system, this configuration is a more common device for the industrial application in comparing with the three-electrode system. Therefore, cathodic deposition of TiO_2 was investigated in both three-electrode and dual-electrode systems. Although Pt is a common counter electrode in the three-electrode design, the dimensionally stable anode (DSA), consisting of a titanium substrate and a binary RuO_2-TiO_2 coating, presents several advantages such as high resistance to corrosion, high chemical stability, high surface area and electrocatalytic activity for industrial applications.[36–38] Since TiO_2 is proposed to be deposited cathodically in this work, DSA is used as the anode in both acidic baths from the consideration of anticorrosion and the high O_2-evolving activity.[39]

Experimental

Titanium dioxide films were cathodically deposited onto Ti foils from two newly developed deposition baths which basically contain 75 mM HCl, 30 mM $TiCl_3$ and 75 mM $NaNO_3$. In preparing bath A, equal-volume 60 mM H_2O_2 was utilized to pre-oxidize 120 mM $TiCl_3$. Then, a 150 mM $NaNO_3$ solution with its volume equal to the above mixture was added and agitated with a stir bar for 30 min when the above mixture became transparent. For bath B, an equal-volume 120 mM $NaNO_3$ was used to replace the solution containing 60 mM H_2O_2 while the other steps are the same. For the EQCM study, the concentration of all species in baths A and B was diluted to 1/50. Electrochemical deposition of TiO_2 was carried out under

*Electrochemical Society Active Member.
zE-mail: cchu@che.nthu.edu.tw

either a three-electrode or a dual-electrode mode by means of cyclic voltammetric (CV), potentiostatic (PS), galvanostatic (GS), and pulse-rest (PR) plating. Note that the total time for deposition under the PS, GS, and PR modes was the same (750 sec; i.e., the total time during the repeated pulse periods is 750 sec). The Ti substrates were pretreated ultrasonically in 6 M HCl for 30 min and deionized water for 10 min, respectively, and dried in a vacuum oven at room temperature. The exposed surface area of Ti foils is 10 mm × 10 mm in this study. The resultant TiO_2/Ti electrodes were rinsed with deionized water for several times and dried in a vacuum oven at room temperature.

In the three-electrode deposition mode, an Ag/AgCl electrode (Argenthal, 3 M KCl, 0.207 V vs. SHE at 25°C) was used as the reference and a piece of platinum gauze was employed as the counter electrode. In the dual-electrode deposition mode, a dimensionally stable anode (DSA) with an exposed surface area of 30 mm × 30 mm is employed. The linear sweep voltammetric (LSV) study and CV deposition were performed by an electrochemical analyzer (CHI 633c, CH Instrument). The scan rate of CV and LSV is equal to 25 mV s^{-1}. In the EQCM study, TiO_2 was deposited onto the Au/Ti-sputtered quartz crystal working electrode in an EQCM cell under the LSV mode. The exposed geometric area of the EQCM electrode for TiO_2 deposition is 0.196 cm^2. The mass of TiO_2 was simultaneously monitored by the quartz crystal microbalance. EQCM responses were conducted by an electrochemical analyzer (CHI 4051a, CH Instruments Inc.) with Ag/AgCl and platinum as the reference and counter electrodes, respectively. All deposition baths were initially agitated at room temperature for 5 min and then kept at the specified temperature for 25 min.

The morphology of TiO_2 films was examined by a field-emission scanning electron microscope (FE-SEM, Hitachi S-4700I). The mass of deposits was determined by a balance (Sartorius AG Göttingen BP-211D) with resolution of 0.01 mg. Two samples were prepared at each temperature and the average mass was reported in this work. The surface roughness is measured by an atomic force microscope (AFM, CSPM 5500). The crystalline phase of annealed TiO_2 was determined by X-ray diffraction (XRD) analysis (Rigaku, Ultima IV). The in-situ UV-VIS absorption spectra were acquired by a UV-VIS spectrophotometer (MultiSpec-1501, SHIMADZU).

Results and Discussion

In-situ UV-VIS absorption spectroscopic analysis—The homogeneous redox reactions between Ti(III) and H_2O_2 as well as between Ti(III) and NO_3^- were examined through the in-situ UV-VIS absorption spectroscopic analysis and typical results are shown in Fig. 1. In Fig. 1a and 1b, H_2O_2 and NO_3^- were respectively added at the 30th and the 27th second, resulting in the presence of fluctuations on their UV-VIS absorption spectra. In Fig. 1a, a strong absorption in the wavelength range below 600 nm is attributable to the formation of orange Ti(VI) species which was over-oxidized from Ti(III) due to presence of localized, concentrated H_2O_2 species when H_2O_2 was added into the $TiCl_3$ solution. Finally, Ti(VI) species should react with Ti(III) to form Ti(IV) because the solution was flashed into transparent. On the other hand, in Fig. 1b, Ti(III) was gradually and completely oxidized to Ti(IV) in ca. 75 seconds when NO_3^- was added into the $TiCl_3$ solution. The possible mechanism responsible for redox reactions between Ti(III) and NO_3^- has been proposed in our previous work:[28,29]

$$Ti^{3+} + NO_3^- \rightarrow TiO^{2+} + NO_2 \tag{7}$$

since reddish-brown NO_2 bubbles are visible in bath B when the $TiCl_3$ solution was mixed with $NaNO_3$. Based on the similar adsorption spectra but a faster rate of the redox reaction between Ti(III) and H_2O_2 in the 200-second measurement, the resultant products formed in the $TiCl_3 + H_2O_2$ solution may be somewhat complicated. The mechanism corresponding to this redox reaction is expressed as follow:[35]

$$Ti^{3+} + H_2O_2 \rightarrow Ti^{4+} + OH^- + OH\cdot \rightarrow TiOH^{3+} + OH\cdot \tag{8}$$

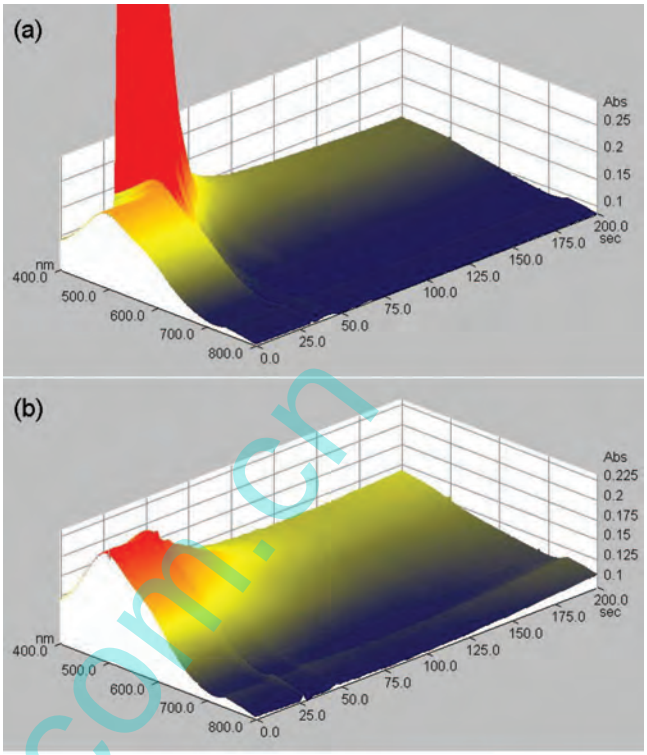

Figure 1. The in-situ UV-VIS adsorption spectra measured from a solution containing 75 mM HCl, 30 mM $TiCl_3$, and (a) 15 mM H_2O_2 and (b) 30 mM $NaNO_3$.

$$Ti^{3+} + OH\cdot \rightarrow Ti^{4+} + OH^- \rightarrow TiOH^{3+} \tag{9}$$

In the redox reaction between $TiCl_3$ and H_2O_2, the oxidized Ti^{4+} has been proved to form a complex coordinated with the hydroxyl radical.[35] Accordingly, olation of hydroxyl Ti(IV) species (i.e., $TiOH^{3+}$) to form dimmers may occur in the solution,[40] which is favorable for the cathodic deposition of TiO_2 (see below):

$$Ti^{3+} + \cdot HOTiOH^{3+} \rightarrow [Ti\overset{(OH)}{\underset{(OH)}{\cdots\cdots}}Ti]^{6+} \tag{10}$$

$$\text{or} \qquad 2TiOH^{3+} \rightarrow [Ti\overset{(OH)}{\underset{(OH)}{\cdots\cdots}}Ti]^{6+} \tag{11}$$

where $\cdots$ indicates two hydrogen bonds formed between metallic and hydroxyl ions. The above differences in the reaction time scale and resultant oxidized products suggest that H_2O_2 is much more active than NO_3^- for the oxidation of Ti(III) to Ti(IV), which will be consumed immediately when it is added in the deposition bath (bath A). In the above two baths for TiO_2 deposition, 15 mM H_2O_2 and 30 mM $NaNO_3$ was added in the basic deposition solution to convert Ti(III) into Ti(IV) meanwhile NO_3^- is the species responsible for the OH^- generation during the cathodic deposition of TiO_2 from both baths. Hence, the generation of concentrated OH^- for TiO_2 deposition in baths A and B is simply expressed as equations (2) and (3) in the less and more negative potential regions, respectively based on the evolution and disappearance of N_2 bubbles.[28,29]

Comparisons of two baths for TiO_2 deposition—Figures 2a and 2b show the typical LSV and Δm-E curves measured at 25 mV s^{-1} from 0 to −1.6 V (vs. Ag/AgCl) in diluted baths A and B, respectively. In Fig. 2a, the onset potential of reduction on both i-E curves is the same, −0.47 V, which is reasonably due to the same reaction, NO_3^- reduction on the EQCM electrode. Since N_2 evolution occurs between −0.6 V and −1.2 V,[28,29] equation (2) should be the main reaction responsible for the OH^- generation. Note that the reduction

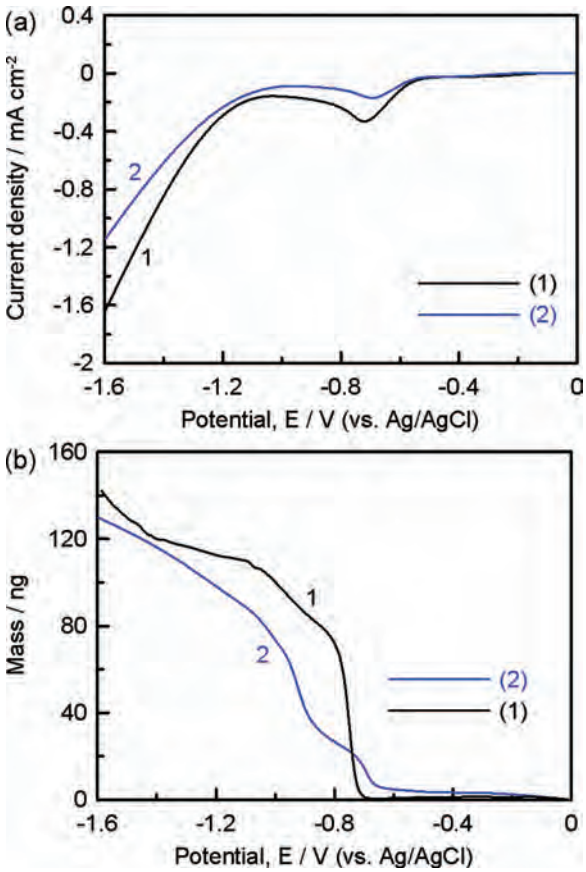

Figure 2. (a) LSV an (b) Δm-E curves measured at 25 mV s^{-1} from 0 to −1.6 V (vs. Ag/AgCl) in a solution containing 1.5 mM HCl, 0.6 mM $TiCl_3$, 1.5 mM $NaNO_3$, and (1) 0.3 mM H_2O_2 and (2) 0.6 mM $NaNO_3$.

currents on curve 1 are always higher than that on curve 2 at any specified potentials negative to −0.47 V although the concentration of NO_3^- in both baths should be the same under the assumption that most NO_2 gases generated in bath B are not dissolved in the deposition bath. Accordingly, the formation of certain Ti(IV) hydroxyl species (e.g., $[Ti\begin{smallmatrix}(OH)\\(OH)\end{smallmatrix}Ti]^{6+}$) in bath A may be favorable for the NO_3^- reduction although the exact reasons responsible for this phenomenon are unclear.

In Fig. 2b, the mass of TiO_2 increases sharply from 0 to 70 ng in the potential region between −0.71 and −0.8 V and then, a gradual increase to 145 ng at potentials negative to −0.8 V on curve 1. On curve 2, significant increase in mass commences at ca. −0.68 V and then, a shoulder is found between −0.68 and −0.9 V. After that, a sharp increase in mass occurs from −0.9 to −1.0 V and a gradual increase from 70 to 130 ng at potentials negative to −1.0 V. Clearly, the TiO_2 deposition rate in bath A is obviously higher than that in bath B, attributable to the formation of Ti(IV) hydroxyl species containing bridged OH groups in the solution. Such Ti(IV) hydroxyl species (with olation) need fewer OH^- to form the polymeric oxy-hydroxyl Ti precipitates which will be converted to TiO_2 through dehydration. Accordingly, the formation of Ti(IV) hydroxyl dimmers containing bridged OH groups is proposed to favor the cathodic deposition of TiO_2. From a comparison of Fig. 2a and 2b, an obvious weight gain is visible when potentials are negative to −0.7 V, suggesting that once the potential is negative enough to accumulate concentrated OH^-, the Ti(IV) species will combine with OH^- to form TiO_2 on the electrode surface.

Since the solutions employed in the EQCM study are diluted, the dependence of TiO_2 mass on the cycle number of CV from baths A and B is used to confirm the above proposal for the enhanced deposition rate in bath A. Lines 1 and 2 in Fig. 3 show the dependence of TiO_2 mass on the cycle number of CV between 0 and −1.6 V from baths A and B, respectively. Clearly, the dependence of TiO_2 mass on the cycle number of CV from both deposition baths is linear. However, the slope of curve 1 is obviously higher than that of curve 2, revealing that the deposition solution containing H_2O_2 is more favorable for the cathodic deposition of TiO_2 in comparison with that containing NO_3^- only, which is identical to the results shown in Fig. 2.

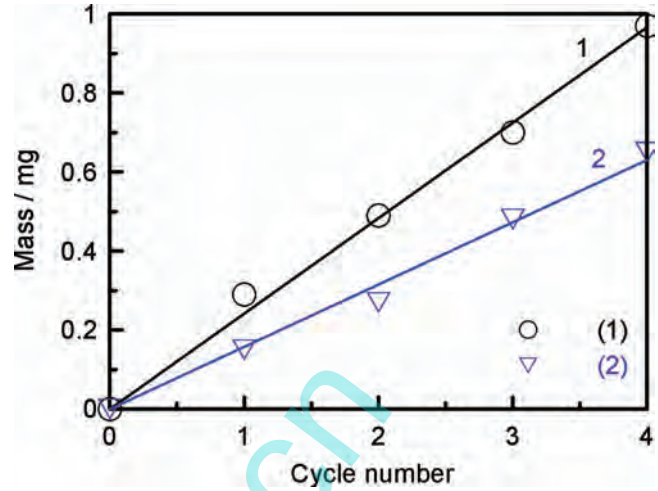

Figure 3. Dependence of TiO_2 mass on the cycle number of CV; TiO_2 was deposited at 25°C from a solution containing 75 mM HCl, 30 mM $TiCl_3$, 75 mM $NaNO_3$, and (1) 15 mM H_2O_2 and (2) 30 mM $NaNO_3$.

The above analyzes reveal that the rate of TiO_2 deposition can be changed by adding 15 mM H_2O_2 to replace 30 mM NO_3^- in bath B while it has to be emphasized here that the role of H_2O_2 in the bath A is different from that in several previous studies.[12,30,41,42] Note that most Ti precursors used in these previous studies are $TiCl_4$ or Ti powders while baths A and B were prepared from $TiCl_3$. Accordingly, H_2O_2 in the previous studies was employed to obtain over-oxidized Ti^{6+} but this work employs the careful oxidation of Ti^{3+} to Ti^{4+} to form the Ti(IV) hydroxyl species, favorable for TiO_2 deposition. Moreover, the over-oxidized Ti species (i.e., Ti^{6+}) must be electrochemically reduced during the deposition process because of the formation of TiO_2 (i.e., Ti^{4+}). However, in baths A and B, Ti^{4+} species (oxidized from Ti^{3+} either by NO_3^- or H_2O_2) do not need to be reduced in order to form TiO_2. Accordingly, baths A and B and the corresponding deposition mechanism should be simpler than those in previous reports. This may be the reason why the rates of TiO_2 deposition in baths A and B are much faster than those reported previously.

The above results and discussion reasonably describe the novelty and advantages of baths A and B meanwhile the rate of TiO_2 deposition can be further enhanced by adding H_2O_2 to replace some NO_3^- in bath B. However, the microstructure of TiO_2 deposits obtained from baths A and B has to be checked in order to consider their future applications. Figures 4a and 4b show the typical surface morphology of two TiO_2 deposits plated from baths A and B, respectively. Note that both deposits have been annealed in air at 400°C for 1 h. From a comparison of Fig. 4a and 4b, the morphologies of TiO_2 deposited from baths A and B are very similar although their deposition rates are undoubtedly different. The particle size of TiO_2 on both films are about 100–150 nm and these particles are aggregates of TiO_2 primary particulates. The appearance of TiO_2 primary particulates becomes clear and spherical after the post-deposition annealing treatment. Note in Fig. 4c that both TiO_2 deposits are highly crystalline after the post-deposition annealing treatment and that the strongest diffraction peak corresponds to the facet (101) of A-TiO_2. Through the Scherrer equation and the full width at half maximum (FWHM) of facet (101), the crystalline size of A-TiO_2 in these primary particulates is about

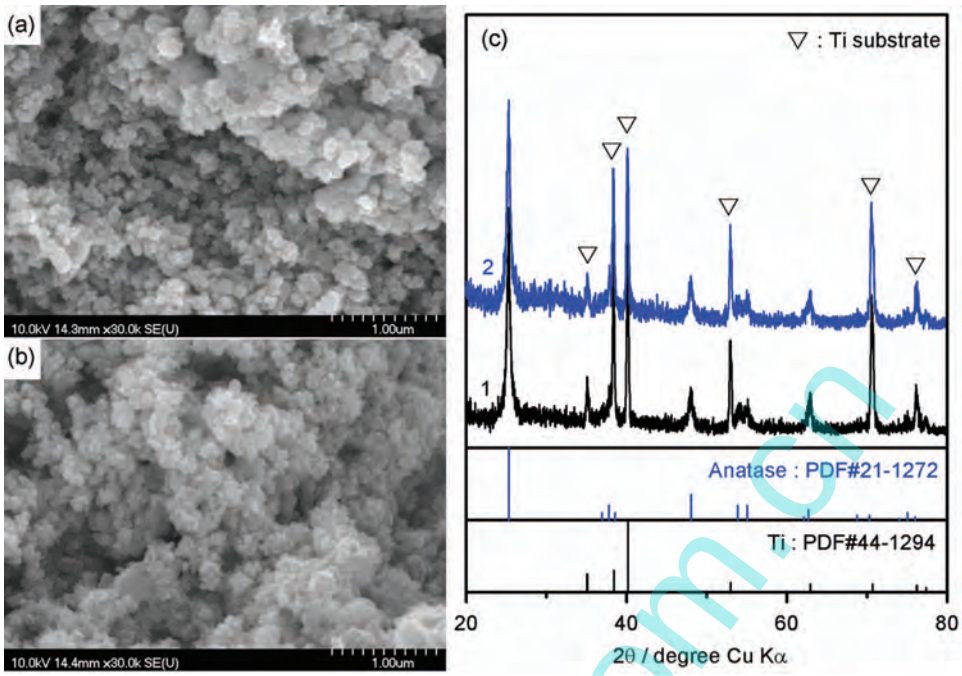

Figure 4. (a,b) SEM images and (c) XRD patterns of TiO_2 deposited at 25°C from a solution containing 75 mM HCl, 30 mM $TiCl_3$, 75 mM $NaNO_3$, and (a,1) 15 mM H_2O_2 and (b,2) 30 mM $NaNO_3$. Both TiO_2 deposits were annealed in air at 400°C for 1 hr.

17.5 nm. Since the chemical precipitation and dehydration of oxy-hydroxyl-Ti species for the formation of TiO_2 are under a similar environment in baths A and B, the crystalline structure of both TiO_2 deposits are reasonably the same. Accordingly, the usage of H_2O_2 in bath A only affects the deposition rate of TiO_2.

Electrochemical characterization of bath A in the dual-electrode system for TiO_2 deposition—Figure 5 shows the typical LSV curve measured through a dual-electrode mode in bath A. Due to the electrochemical polarization on both anode and cathode, the electrochemical reduction of NO_3^- commences at ca. −1.5 V, which is much more negative than the onset potential of NO_3^- reduction obtained in the three-electrode system. On the other hand, from a comparison of Fig. 2a and Fig. 5, the electrochemical responses measured under this dual-electrode mode are similar to that obtained in the three-electrode mode under the understanding of the combined polarization on both anode and cathode in the dual-electrode system. Accordingly, based on our previous work,[28] the two reduction peaks at −2.5 and −2.8 V in Fig. 5 are attributable to the electrochemical reduction of NO_3^- while the hydrogen evolution reaction becomes the predominant reaction at potentials negative to −3.0 V. Therefore, the potential region between −1.5 and −3 V is expected to effectively deposit TiO_2 in the dual-electrode system if the electrochemical reduction of NO_3^- is set as the exclusive source for the OH^- generation. Based on this LSV curve, −0.025 A cm^{-2} and −2.6 V are employed in the GS and PS deposition modes, respectively.

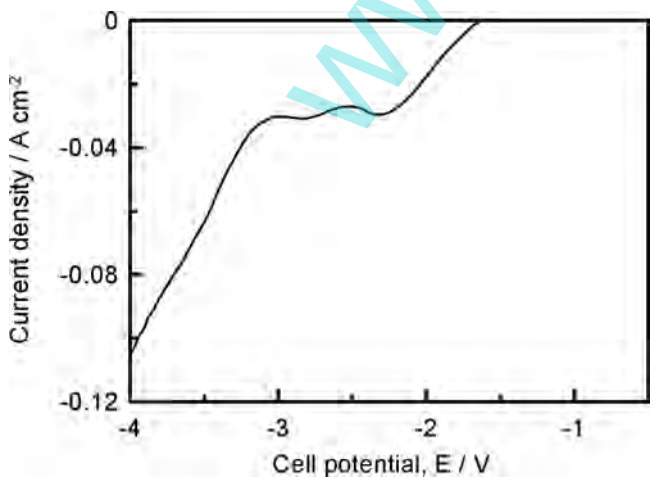

Figure 5. A LSV curve measured at 25 mV s^{-1} from a cell voltage of −0.5 V to −4 V in a solution containing 75 mM HCl, 30 mM $TiCl_3$, 75 mM $NaNO_3$, and 15 mM H_2O_2.

Effects of deposition modes in the dual-electrode system for TiO_2 deposition—From the consideration of deposition modes, there is only one parameter can be chosen in direct current (DC) electrolysis, namely cell voltage or current density. Whereas in the PR mode, the additional parameters, pulse time (t_{on}) and rest time (t_{off}), can be varied independently, which provide a variety in the mass transport situation, electrode kinetics, and nucleation overpotential.[43,44] Moreover, the duty percentage (DP) and pulse frequency (PF) are defined as below:[45,46]

$$\text{Duty percentage(DP)} = \frac{t_{on}}{t_{on} + t_{off}} \times 100\% \quad (12)$$

$$\text{Pulse frequency(PF)} = \frac{1}{t_{on} + t_{off}} \quad (13)$$

Due to the multiple parameters, the PR mode generally shows several advantages such as stronger adhesion, uniform deposits, and controllable particle size of deposits in comparison with the DC mode. In the DC mode, the consuming rate of NO_3^- is expected to be directly proportional to the current density in the potential region between −1.5 and −3 V. The highest steady-state current density achieved in this potential region should be the limiting current density of NO_3^- reduction; i.e., the interfacial concentration of NO_3^- is close to 0 and a steady-state concentration gradient of NO_3^- is established. Here, the PR mode can considerably enhance the limiting current density because diffusion and natural convection of NO_3^- during the rest period will increases the interfacial concentration of NO_3^-.[47] The higher limiting current density of NO_3^- reduction will generate more concentrated OH^- at the vicinity of the electrode-electrolyte interface,

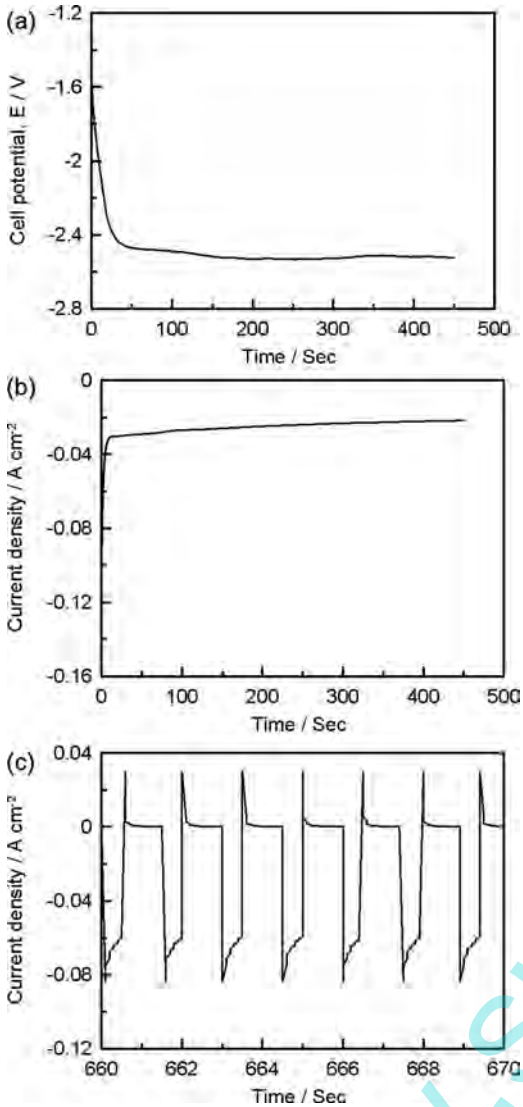

Figure 6. (a) V-t curve measured at 25 mA cm^{-2}, (b) i-t curve measured at a cell voltage of −2.6 V, and (c) i–t curve of PR deposition (the pulse cell voltage = −2.6 V, t_{on} = 0.5 sec and t_{off} = 1 sec) measured at 25°C from a solution containing 75 mM HCl, 30 mM $TiCl_3$, 75 mM $NaNO_3$, and 15 mM H_2O_2.

resulting in a faster rate or even a different nucleation mechanism or growth mode of TiO_2 deposition in comparing with the DC mode. Similarly, the exhaustion of Ti ions at the electrolyte-electrode interface can be efficiently supplied from the bulk solution during the rest period. Accordingly, under the PR mode, restrictions in the generation of concentrated OH^- and the formation of TiO_2 precipitates at the vicinity of the electrode-electrolyte interface are expected to be low and the operation window for depositing TiO_2 is effectively extended.

Typical electrochemical responses for preparing TiO_2 deposits under the GS, PS, and PR modes are shown as Fig. 6a–6c, respectively. The GS method guarantees a constant reduction rate of NO_3^- when the applied current density is lower than the limiting current density. This constant OH^- generation rate may result in a constant deposition rate of TiO_2. Note in Fig. 6a that when the applied current density is equal to −25 mA cm^{-2}, the cell voltage starts at −1.62 V, decreases gradually to −2.43 V in the initial 27 seconds, and then, a quasi-steady-state potential of NO_3^- reduction, equal to ca. −2.5 V, is obtained. This quasi-steady-state potential is close to the applied potential in the PS deposition (−2.6 V). In Fig. 6b, due to the double-layer charging effect and the much higher NO_3^- concentration gradient in the initial reduction stage, a much higher reduction current density, ca. 98 mA cm^{-2}, is obtained, which drops sharply to ca. −30 mA cm^{-2} within 12 seconds, reasonably attributed to the absence of double-layer charging current and the dramatic decrease in the NO_3^- concentration gradient. Then, the current density decreases slowly to a steady state value, ca. −25 mA cm^{-2}. The gradual decrease in the current density may be due to the significant iR drop through the TiO_2 film already deposited onto the substrate. Figure 6c shows the i-t responses under the PR deposition mode in which the pulse potential and the ratio of pulse/rest time are equal to −2.6 V and 0.5/1 (in second), respectively. There are obvious pulse currents at the transition of pulse time and rest time. In addition, the current density in the pulse period is always much larger than 60 mA cm^{-2}. This phenomenon is attributable to the diffusion of reacting species (e.g., NO_3^-) to the vicinity of the electrolyte-electrode interface during the rest period, significantly increasing the current density in the pulse period. Accordingly, the above result clearly reveals that the PR mode considerably enhances the limiting current density of NO_3^- reduction in comparison with the DC mode (e.g., the PS deposition mode). Therefore, the operation window for the cathodic deposition of TiO_2 can be effectively extended.

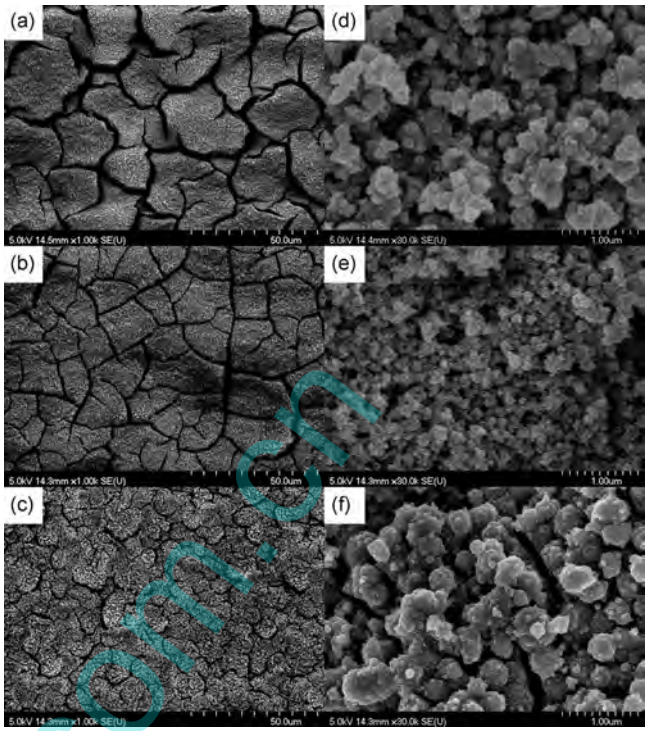

Figure 7. SEM images of TiO_2 deposits prepared under (a,d) a constant applied current density, 25 mA cm^{-2}; (b,e) a constant cell voltage of −2.6 V, and (c) PR mode (the pulse cell voltage = −2.6 V, t_{on} = 0.5 sec and t_{off} = 1 sec) at 25°C from a solution containing 75 mM HCl, 30 mM $TiCl_3$, 75 mM $NaNO_3$, and 15 mM H_2O_2.

Figure 7 shows the surface morphologies of TiO_2 deposits prepared by means of GS, PS, and PR deposition modes (denoted as TiO_2-GS, TiO_2-PS, and TiO_2-PR, respectively). Note that TiO_2 can be deposited under the dual-electrode system from both baths A and B while a faster deposition rate is obtained in bath A. Hence, bath A is employed in this section. From Fig. 7a and 7b, the surface of TiO_2-GS and TiO_2-PS deposits are dense and compact although large cracks are clearly visible on both deposits. Although the deposition conditions of GS and PS modes are very similar according to Figure 6, the surface of TiO_2-PS is more uniform and the particle size is smaller from a comparison of Figures 7d and 7e. However, poor adhesion of TiO_2-PS is an important issue. The surface of TiO_2-PR shows much smaller cracks (Figure 7c) and the best adhesion among the above

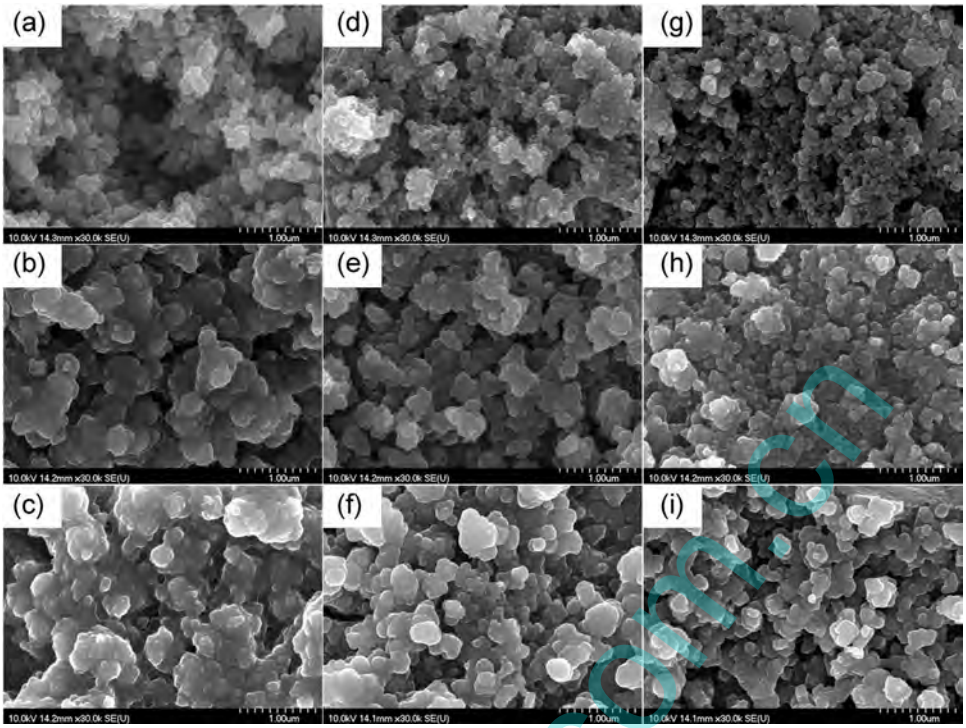

Figure 8. SEM images of TiO_2-PR prepared at a pulse cell voltage of −2.6 V with (t_{on}, t_{off}) = (a) (0.25, 0.5) (b) (0.25, 1), (c) (0.25, 2), (d) (0.5, 0.5) (e) (0.5, 1), (f) (0.5, 2), (g) (1, 0.5) (h) (1, 1), and (i) (1, 2) sec at 25°C from a solution containing 75 mM HCl, 30 mM $TiCl_3$, 75 mM $NaNO_3$, and 15 mM H_2O_2.

three deposits, suggesting the lowest stress in the TiO_2-PR deposit. However, the particle size seems to be the largest among the above three deposits (Figure 7f) although the particles on all deposits can be considered as aggregates of TiO_2 primary particulates. Based on the above results and discussion, the PR mode is considered as a suitable strategy for mass production of TiO_2 films in the industrial applications.

Effects of PR deposition parameters on the microstructure of TiO_2—Figure 8 shows the SEM images of TiO_2-PR prepared at a pulse potential of −2.6 V with the pulse time ranging from 0.25 to 1 sec and the rest time varying from 0.5 to 2 sec at 25°C. In general, all TiO_2-PR deposits show a uniform but rough surface morphology meanwhile, different values of t_{on} and t_{off} lead to different surface morphologies, indicating that the ratio of t_{on}/t_{off} significantly affects the nucleation and growth of TiO_2. The aggregate size of TiO_2 primary particulates gradually decreases as t_{on} increases while opposite results are obtained when t_{off} increases. The above results demonstrate that the surface morphology of TiO_2 deposits can be finely tuned by independently varying t_{on} and t_{off}. Moreover, from AFM analyzes, the root-mean-square (rms) roughness is 86.7, 85.3, 112, 47.5, 84.5, 75.1, 41.3, 65.9, and 56 nm for Fig. 8a–8i, respectively. Clearly, as t_{on} increases, the rms roughness of TiO_2 decreases (e.g., 86.7, 47.5, and 41.3 nm for t_{off} = 0.5 sec, t_{on} = 0.25, 0.5, and 1 sec, respectively), further revealing a smoother and more uniform TiO_2 film obtained at a longer t_{on} period. However, there is no regularity in the surface roughness with changing t_{off}, which is attributable to the original concentration of Ti^{4+} at the vicinity of the cathode-electrolyte interface is abundant under the PR mode with a short pulse time. Hence, the effect of Ti^{4+} diffusion on the surface roughness is minor. Accordingly, the amount of OH^- generated at the cathode-electrolyte interface during the t_{on} period is proposed to be the key factor affecting the surface roughness of TiO_2. The above proposal suggests that the great amount of OH^- formed at the cathode vicinity generally results in a rapid precipitation of TiO_2 on the cathode surface. Meanwhile, during t_{off}, Ti^{4+} keeps reacting with concentrated OH^- generated within t_{on}, and the uniform morphology of resultant TiO_2 particles should result from rearrangement of oxy-hydroxyl-Ti species. Accordingly, a smoother TiO_2 deposit is obtained with prolonging t_{on} although the exact reasons responsible for the above phenomenon are still unclear.

Note that the freshly prepared TiO_2 deposits are of an amorphous structure while crystalline TiO_2 generally shows better electrical conductivity. Therefore, annealing in air at elevated temperatures is inevitable to obtain a well-crystalline TiO_2 deposit. In this work, annealing in air for 1 h at 400°C renders the significant crystallization of TiO_2 which shows a pure anatase phase (not shown here). Moreover, from the Scherrer equation, the average crystal size of annealed TiO_2 is equal to 8.4, 7.9, 6.0, 8.5, 8.1, 7.5, 10.7, 9.2, and 7.9 nm for Fig. 8a–8i, respectively. Clearly, the average crystal size slightly increases with increasing t_{on} (e.g., 8.4, 8.5, and 10.7 nm for t_{off} = 0.5 sec, t_{on} = 0.25, 0.5, and 1 sec, respectively). This phenomenon is probably due to the formation of smaller primary TiO_2 particulates with a longer t_{on}, favorable the growth of TiO_2 nanocrystallites.

Figure 9 shows the typical SEM images of TiO_2-PR prepared at a pulse potential of −2.6 V with varying PF (pulse frequency) and DP (duty percentage). As mentioned in proposing equations (12) and (13), the PF and DP are important parameters in the PR deposition. Here, DPs are kept at 66.7, 33.3, and 11.1% meanwhile PFs equal to 100 and 10 Hz are applied to each DP setting. From a comparison of Fig. 9a and 9d (also for 9b and 9e or 9c and 9f), the deposit prepared under a PF of 100 Hz generally shows a looser structure than that prepared under a PF of 10 Hz. Since the double-layer effect becomes very significant with increasing PF due to shorter t_{on} and t_{off}, the high pulse current density applied to charging/discharging the electrical double layer under a high PR should promote the migration of ions (e.g., Ti^{4+} and OH^-) at the cathode-electrolyte interface. This phenomenon should result in a porous and looser deposit. From a comparison of Fig. 9a–9c (or 9d–9f), the particle size of TiO_2 aggregates decreases with increasing the DP value. Since PR deposition with high DP values will approach a PS deposition mode,[45,46] the SEM images in Fig. 9a and 9d are very similar to that shown in Fig. 6e for a TiO_2-PS deposit. From all the above results and discussion, the microstructure (e.g., surface morphology, aggregate size, and surface

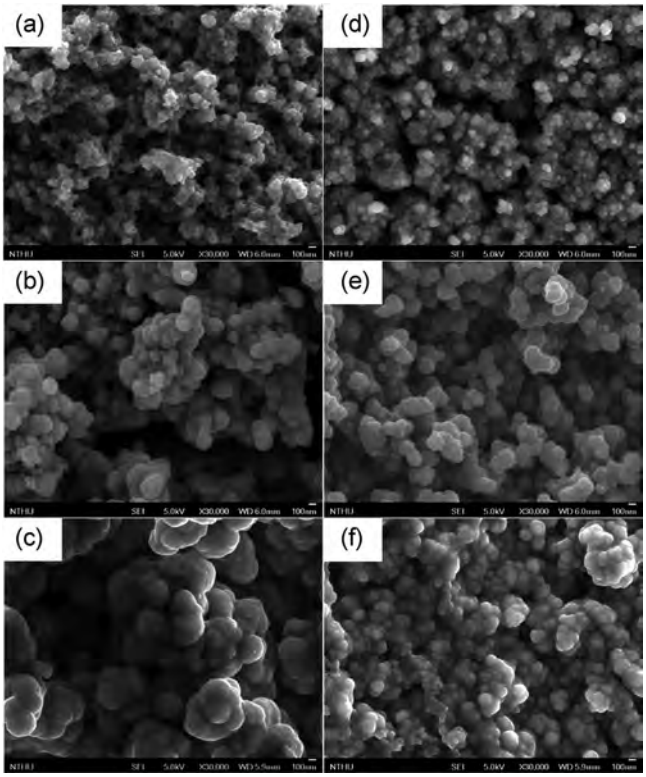

Figure 9. SEM images of TiO_2-PR prepared at a pulse cell voltage of −2.6 V with the pulse frequency of (a-c) 100 and (d-f) 10 Hz and the duty percentage of (a,d) 66.7, (b,e) 33.3 and (c,f) 11.1% at 25°C from a solution containing 75 mM HCl, 30 mM $TiCl_3$, 75 mM $NaNO_3$, and 15 mM H_2O_2.

roughness) of TiO_2 deposits can be effectively tuned by independently varying the deposition parameters of the PR mode, such as DP and PF.

Conclusions

The EQCM and CV results reveal that the deposition solution containing H_2O_2 exhibits a higher rate of TiO_2 deposition in comparison with the solution containing $NaNO_3$, probably due to the formation of Ti(IV) hydroxyl species in the former bath. Although the rate of TiO_2 deposition is enhanced by introducing H_2O_2, the resultant deposits show similar morphologies and an amorphous structure of TiO_2. Pure anatase TiO_2 nanocrystals can be obtained by an annealing treatment in air at 400°C for 1 h. The newly developed solution has been successfully used in the dual-electrode deposition system and the surface morphology of TiO_2 deposits can be controlled by varying the deposition mode. Moreover, the microstructure (e.g., surface morphology, aggregate size, and surface roughness) of TiO_2 can be effectively tuned by independently varying the pulse-rest deposition parameters, such as t_{on} and t_{off} as well as pulse frequency and duty percentage.

Acknowledgments

The financial support of this work, by the National Science Council of the Republic of China and the boost program from the Low Carbon Energy Research Center of NTHU, is gratefully acknowledged.

References

1. A. Fujishima, T. N. Rao, and D. A. Tryk, *Electrochim. Acta*, **45**, 4683 (2000).
2. A. L. Linsebigler, G. Q. Lu, and J. T. Yates, *Chem. Rev.*, **95**, 735 (1995).
3. X. Chen and S. S. Mao, *Chem. Rev.*, **107**, 2891 (2007).
4. B. Oregan and M. Gratzel, *Nature*, **353**, 737 (1991).
5. A. Hagfeldt and M. Gratzel, *Acc. Chem. Res.*, **33**, 269 (2000).
6. D. Li and Y. N. Xia, *Nano Lett.*, **3**, 555 (2003).
7. D. Gong, C. A. Grimes, O. K. Varghese, W. Hu, R. S. Singh, Z. Chen, and E. C. Dickey, *J. Mater. Res.*, **16**, 3331 (2001).
8. J. M. Macák, H. Tsuchiya, A. Ghicov, and P. Schmuki, *Electrochem. Commun.*, **7**, 1133 (2005).
9. K. Wessels, M. Minnermann, J. Rathousky, M. Wark, and T. Oekermann, *J. Phys. Chem. C*, **112**, 15122 (2008).
10. L. Kavan, B. O'Regan, A. Kay, and M. Gratzel, *J. Electroanal. Chem.*, **346**, 291 (1993).
11. K. Wessels, A. Feldhoff, M. Wark, J. Rathousky, and T. Oekermann, *Electrochem. Solid-State Lett.*, **9**, C93 (2006).
12. C. Natarajan and G. Nogami, *J. Electrochem. Soc.*, **143**, 1547 (1996).
13. G. Zotti, G. Schiavon, and S. Zecchin, *J. Electrochem. Soc.*, **146**, 637 (1999).
14. K. Kamada, M. Mukai, and Y. Matsumoto, *Electrochim. Acta*, **47**, 3309 (2002).
15. S. Karuppuchamy, K. Nonomura, T. Yoshida, T. Sugiura, and H. Minoura, *Solid State Ionics*, **151**, 19 (2002).
16. A. M. Peiro, E. Brillas, J. Peral, X. Domenech, and J. A. Ayllon, *J. Mater. Chem.*, **12**, 2769 (2002).
17. C. D. Lokhande, S. K. Min, K. D. Jung, and O. S. Joo, *J. Mater. Sci.*, **39**, 6607 (2004).
18. I. Zhitomirsky and L. GalOr, *J. Euro. Ceram. Soc.*, **16**, 819 (1996).
19. S. A. Kumar, P. H. Lo, and S. M. Chen, *Nanotechnol.*, **19**, 255501 (2008).
20. D. M. Macarthur, *J. Electrochem. Soc.*, **117**, 422 (1970).
21. V. Gupta, T. Kusahara, H. Toyama, S. Supta, and N. Miura, *Electrochem. Commun.*, **9**, 2315 (2007).
22. M. Izaki and T. Omi, *Appl. Phys. Lett.*, **68**, 2439 (1996).
23. L. Xu, Y. Guo, Q. Liao, J. Zhang, and D. Xu, *J. Phys. Chem. B*, **109**, 13519 (2005).
24. A. Goux, T. Pauporté, J. Chivot, and D. Lincot, *Electrochim. Acta*, **50**, 2239 (2005).
25. Y. Ishikawa and Y. Matsumoto, *Electrochim. Acta*, **46**, 2819 (2001).
26. S. Karuppuchamy, D. P. Amalnerkar, K. Yamaguchi, T. Yoshida, T. Sugiura, and H. Minoura, *Chem. Lett.*, **1**, 78 (2001).
27. S. T. Chang, I. C. Leu, and M. H. Hon, *J. Crys. Grow.*, **273**, 195 (2004).
28. C. C. Huang, H. C. Hsu, C. C. Hu, K. H. Chang, and Y. F. Lee, *Electrochim. Acta*, **55**, 7028 (2010).
29. C. C. Hu, C. C. Huang, and K. H. Chang, *Electrochem. Commun.*, **11**, 434 (2009).
30. I. Zhitomirsky, *J. Euro. Ceram. Soc.*, **19**, 2581 (1999).
31. B. Xue, R. Liu, and Z. D. Xu, *Mater. Lett.*, **63**, 2377 (2009).
32. I. Zhitomirsky, *Nanostructured Mater.*, **8**, 521 (1997).
33. P. Tengvall, I. Lundström, L. Sjöqvist, H. Elwing, and L. M. Bjursten, *Biomater.*, **10**, 166 (1989).
34. J. Ragai, *Nature*, **325**, 703 (1987).
35. Y. S. Chiang, J. Craddock, D. Mickewich, and J. Turkevich, *J. Phys. Chem.*, **70**, 3509 (1966).
36. R. M. G. de Lima, W. G. R. da Silva, J. W. da Cunha, and J. C. Afonso, *J. Hazard. Mater.*, **161**, 1560 (2009).
37. S. Trasatti, *Electrochim. Acta*, **45**, 2377 (2000).
38. J. C. Forti, P. Olivi, and A. R. de Andrade, *Electrochim. Acta*, **47**, 913 (2001).
39. T. C. Wen and C. C. Hu, *J. Electrochem. Soc.*, **139**, 2158 (1992).
40. M. R. Grace and L. Spiccia, *Inorg. Chim. Acta*, **213**, 103 (1993).
41. I. Zhitomirsky, *Mater. Lett.*, **33**, 305 (1998).
42. C.-M. Lin and S.-K. Yen, *J. Electrochem. Soc.*, **151**, D127 (2004).
43. C. Kollia, N. Spyrellis, J. Amblard, M. Froment, and G. Maurin, *J. Appl. Electrochem.*, **20**, 1025 (1990).
44. N. Ibl, J. C. Puippe, and H. Angerer, *Surf. Technol.*, **6**, 287 (1978).
45. Y. D. Tsai and C. C. Hu, *J. Electrochem. Soc.*, **158**, D482 (2011).
46. Y. D. Tsai, C. Y. Yu, C. C. Hu, and J. G. Duh, *J. Electrochem. Soc.*, **159**, D108 (2012).
47. K. H. Choi, H. S. Kim, and T. H. Lee, *J. Power Sources*, **75**, 230 (1998).